

Flow characteristic of a multistage radial turbine for supercritical compressed air energy storage system

Proc IMechE Part A:
J Power and Energy
0(0) 1–19
© IMechE 2017
Reprints and permissions:
sagepub.co.uk/journalsPermissions.nav
DOI: 10.1177/0957650917743366
journals.sagepub.com/home/pia



Xing Wang¹, Wen Li¹, Xuehui Zhang¹, Yangli Zhu¹, Wei Qin²
and Haisheng Chen¹

Abstract

Compressed air in supercritical compressed air energy storage system expand from supercritical to atmospheric conditions at lower inlet temperature (<500 K) to generate MW scale power. Therefore, a new multistage radial turbine is adopted and the flow characteristic is investigated by numerical simulation. Effects of ideal gas model and tip clearance on the performance and flow field of the multistage turbine are revealed. Results show that ideal gas model can reveal flow pattern under supercritical condition correctly while leading to obvious deviation of isentropic enthalpy drop, entropy, and inlet-to-exit total temperature ratio. Relative differences for mass flow and efficiency are less than 2%, while the relative differences for output power reaches to 9.36%. For shrouded rotor, mixing of working fluid near hub, blade suction surface, and shroud is the main influencing factor of the flow loss in the rotor. For unshrouded rotor, leakage vortex promote mixture of the fluid deriving from the hub, shroud, and suction surface, and causes much higher flow loss in the channel of rotor. The rotors, which have higher blade height variation rate, present higher efficiency reduction when the tip clearance height is increased, which is because the proportion of tip clearance in blade inlet height increases with the increase of average aspect ratio, resulting in the increase of leakage flow at the leading edge of rotor blade. The pressure fluctuation near the tip clearance and efficiency reduction is also increased. The present study provides a reference for further design and optimization of the multistage radial turbines in compressed air energy storage.

Keywords

Compressed air energy storage, multistage, radial turbine, computational fluid dynamics

Date received: 26 May 2017; accepted: 28 September 2017

Introduction

Compressed air energy storage (CAES) is a significant technology for energy storage, as it achieves peak power regulation while overcoming the instability of wind and solar energy, which would otherwise hinder energy utilization. These advantages have led to increasing adoption of the CAES system in modern grids,¹ renewable energy,² waste heat utilization,³ and other fields. The basic workflow of the CAES system is simple.⁴ Electrical energy is converted by compressed air from compressors into potential energy. Then, compressed air stored in the tank is released and expanded through the expander to generate electricity again.

As a key component for the expansion process in CAES, the radial turbine, which has a high expansion ratio and a compact structure⁵ is suitable for the CAES system. The internal flow structure, which influences the aerodynamic performance of radial

turbines, also plays an important role in the efficiency of CAES system. Therefore, many studies have focused on the internal flow structure of radial turbines.

Previous studies have shown that the internal flow structure in radial turbines, which always interact with each other, are complex and varied. An additional single vortex called the “inflow vortex” was observed by Putra and Joos⁶ when they investigated the secondary flow phenomena in a radial turbine nozzle. Zangeneh-Kazemi et al.⁷ analyzed the flow through a rotor of a radial turbine using a fully

¹Institute of Engineering Thermophysics, Chinese Academy of Sciences, Beijing, PR China

²Institute of Mechanics, Chinese Academy of Sciences, Beijing, PR China

Corresponding author:

Haisheng Chen, Institute of Engineering Thermophysics, Chinese Academy of Sciences, 11 Beisihuanxi Road, Beijing 100190, PR China.
Email: chen_hs@mail.etp.ac.cn

three-dimensional viscous solver, and found that the secondary flow was not only one factor influencing the wake flow pattern. Dai and Chen⁸ analyzed the inside flow of radial micro-gas turbine rotors and revealed that tip leakage flow and corner vortex developed and mixed with the main flow through the passage.

Numerous factors, such as geometry and operating condition, also have great effect on the flow structures of the radial turbine. Simpson⁹ compared the loss generation between radial turbines with vaned stators and vaneless volutes under the same operating conditions. Vaneless turbine stators incur lower losses than the corresponding vaned stators, but deliver a higher level of uniformity in the rotor inlet pressure field. Binder et al.¹⁰ analyzed the effects of variable geometry on radial turbines and determined that the geometric configuration of the stator selected to reach a specific value of the reduced section influences the efficiency of the stage. He et al.¹¹ investigated the backface clearance flow in deeply scalloped radial turbines and observed that the increase in the clearance height decreases the heat transfer coefficient caused by the impingement of the scraping flow, but increases the leakage loss. Li et al.¹² conducted a numerical investigation of the three-dimensional flows in a rotor of a radial turbine and observed that the interaction and mixing between passage vortex and tip leakage vortex was the major factor influencing flow loss formation under the design conditions. However, flow separation and backflow of the mean flow occurring at the leading edge caused the majority of flow loss under the off-design conditions. For a microradial inflow turbine,¹³ the flow loss in rotors passage is mainly caused by stagnation of the air flow near the inlet of the impeller and boundary layer friction loss and the loss of wake vortex near the trailing edge of the impeller.

Tip clearance is also one of the key factors affecting the flow field, energy transfer, work capacity, and efficiency of radial turbine. Amedick and Simon¹⁴ simulate the internal flow in a radial turbine rotor. Their results illustrated that the wake and nonuniform flow at outlet of the rotor not only affected by the accumulation of the low kinetic energy fluid, but also influenced by the tip clearance leakage flow, which Deng et al.¹⁵ investigated the effects of rotor blade tip clearance on total aerodynamic performance in a radial inflow turbine, and reveal that radial clearance increases at the rotor exit have about 8.3 times the effect on stage efficiency.

In the present study, the supercritical air is employed to reduce site area and increase the energy density of CAES system,¹⁶ so the compressed air in the multistage radial turbine expands from supercritical to atmospheric conditions to obtain higher output power, which differs from the ordinary operating condition of radial turbines (Figure 1).^{16–23} In addition, radial turbines, which are shrouded and unshrouded

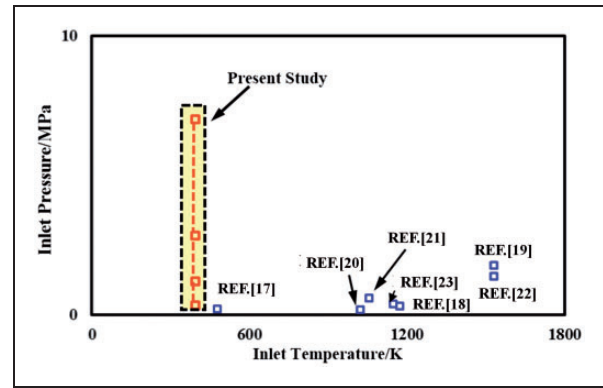


Figure 1. Total pressure and temperature at the inlet of radial turbine.

rotors with different blade profile, are all included in the multistage radial inflow turbine to meet the requirement of operation condition, thus it is difficult for the engineers to determine the stage that has higher flow loss to conduct performance improvement. Although some studies²⁴ has been conducted on the aerodynamic performance and internal flow patterns of multistage radial inflow turbine, the effects of supercritical condition and geometric parameters on the aerodynamic performance and flow characteristic of multistage radial turbine in CAES system is also still not revealed.

In the present study, influence of ideal gas model on the aerodynamic performance and internal flow structure of supercritical radial turbine is analyzed. Effects of tip clearance on the four radial inflow turbines are also revealed. These results above will provide a reference for the further development of high-efficiency radial turbines in CAES.

Description of the multistage turbo-expanders

The scheme of the multistage radial-turbine system adopted in the CAES is depicted in Figure 2. Stages 1 and 2 are installed on a same rotational axis, whereas stages 3 and 4 are installed on another. These four radial turbines are integrated into one multistage radial turbine through a gear box to generate work output together. Each radial turbine is connected through a pipe, and a preheater is also included to increase inlet temperature of radial turbine. A collection chamber is adopted at inlet of radial turbine to ensure uniformity of the air flow. The inlet total pressure and rotational speed for each stage is shown in Table 1.

The sketch of the radial inflow rotor adopted in the present work is shown in Figure 3. The detailed geometric parameters are shown in Table 1. A new geometry parameter χ , which is defined as the ratio of blade height difference ($l_{out} - l_{in}$) to rotor axial length l_{Axial} , is adopted in the present study. This parameter is used to evaluate the variation rate of blade height from

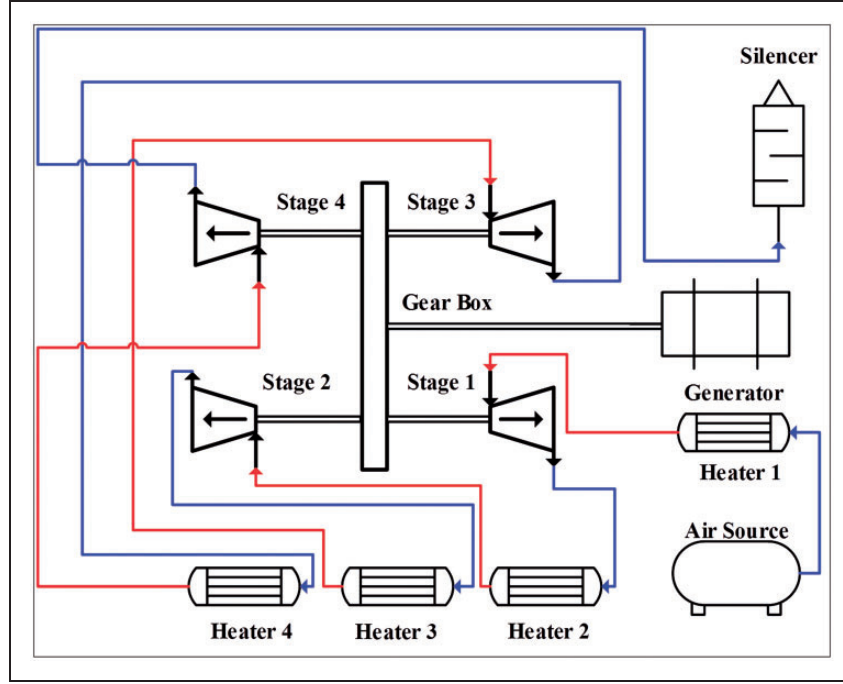


Figure 2. Scheme of the multistage radial inflow turbine system.

Table 1. Parameters of radial inflow turbine.

| Parameters | Stage 1 | Stage 2 | Stage 3 | Stage 4 |
|--------------------------------------|---------|---------|---------|---------|
| Inlet total pressure, P_{in} (MPa) | 7.00 | 2.80 | 1.20 | 0.40 |
| Rotational speed, n (r/min) | 40,000 | 40,000 | 20,000 | 20,000 |
| Rotor inlet diameter, D_{in} (mm) | 135 | 135 | 305 | 305 |
| Rotor axial length, l_{Axial} (mm) | 34 | 34 | 70 | 70 |
| χ | 0.10 | 0.40 | 0.13 | 0.53 |

inlet to outlet of rotor. The detailed definition of χ is given in the following equation

$$\chi = \frac{(l_{out} - l_{in})}{l_{Axial}} \quad (1)$$

where l_{in} is the blade inlet height; l_{out} is the blade outlet height; l_{Axial} is the blade average arc length from inlet to outlet.

As shown in Figure 3, it can be found that the rotor blades in stages 2 and 4 present higher value of χ . It means that these rotors have higher variation rate of blade height from inlet to outlet of rotor.

Numerical method

Three-dimensional model with single channel is adopted in the present study for each stage. Figure 4 shows the numerical model of the four radial turbines. Considering that collection chambers are adopted for the radial inflow turbines, uniform total pressure,

uniform total temperature, and flow angles are specified at the inlet of the model. The average static pressure is specified at the outlet of the model. The inlet turbulence intensity is set to 5%. The rotation speed of the rotors is set based on the requirements of the operating conditions. The interface between rotating and stationary parts is the “stage interface”.

The ANSYS CFX solver is adopted to conduct steady-state 3D viscous compressible flow simulations, and $k-\omega$ shear stress transport (SST) turbulence model is used because of its better ability to solve flow separations and adverse gradients in a typical turbomachinery case.

The mass, momentum, and energy conservation equations solved in the present study are written as follows²⁵

$$\frac{\partial \rho}{\partial t} + \nabla \cdot (\rho \vec{U}) = 0 \quad (2)$$

$$\frac{\partial (\rho \vec{U})}{\partial t} + \nabla \cdot (\rho \vec{U} \otimes \vec{U}) = -\nabla p + \nabla \cdot \tau + \vec{S}_M \quad (3)$$

where the stress tensor, τ , is related to the strain rate by

$$\tau = \mu \left(\nabla \vec{U} + (\nabla \vec{U})^T - \frac{2}{3} \delta \nabla \cdot \vec{U} \right) \quad (4)$$

The total energy equation is described as follows

$$\frac{\partial (\rho h_{tot})}{\partial t} - \frac{\partial p}{\partial t} + \nabla \cdot (\rho \vec{U} h_{tot}) = \nabla \cdot (\lambda \nabla T) + \nabla \cdot (\vec{U} \cdot \tau) + \vec{U} \cdot \vec{S}_M + \vec{S}_E \quad (5)$$

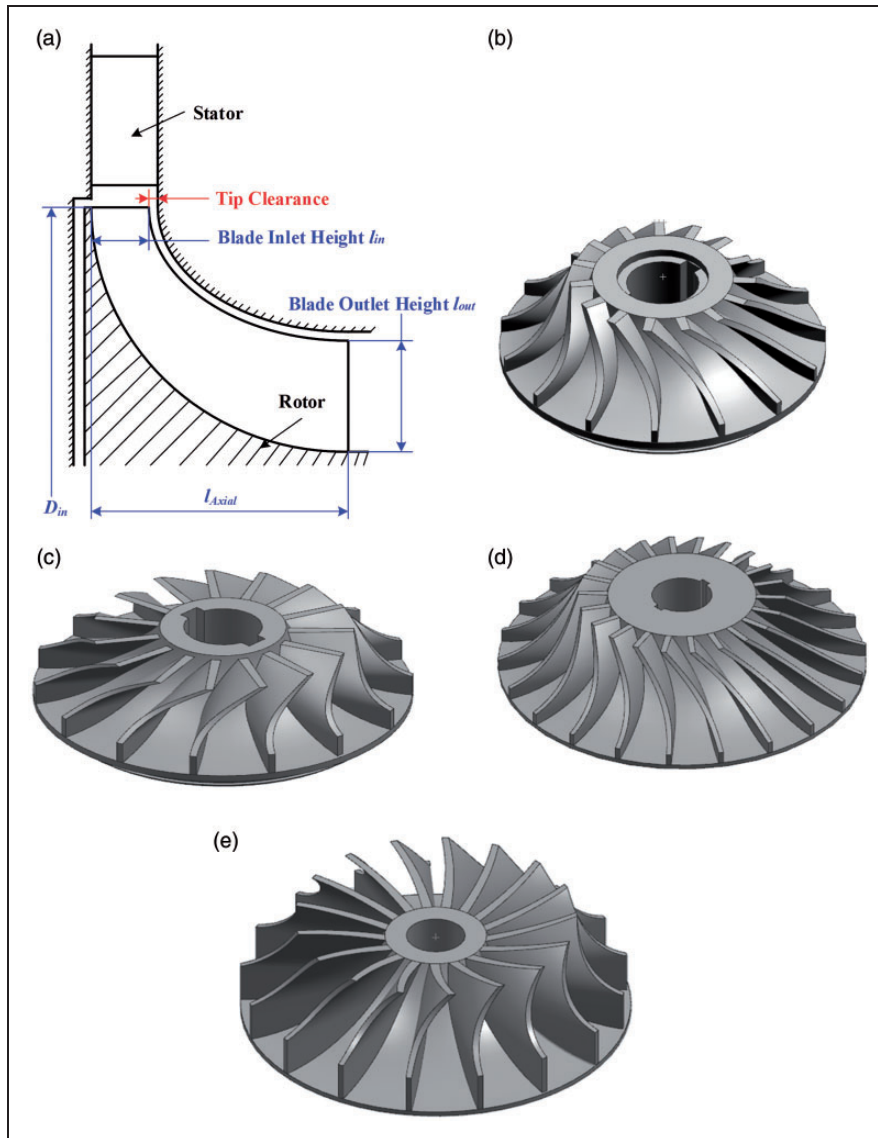


Figure 3. Sketch of the radial inflow rotor: (a) definition of geometry parameters; (b) stage 1; (c) stage 2; (d) stage 3; (e) stage 4.

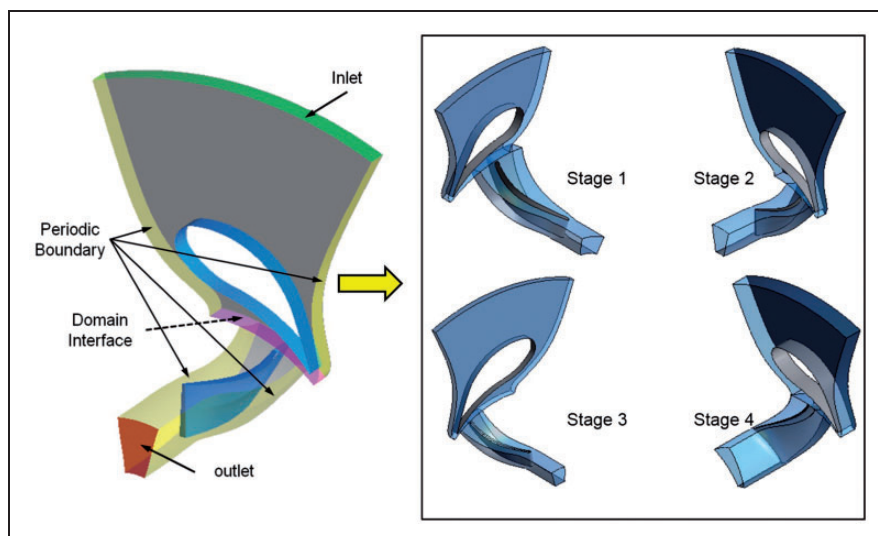


Figure 4. Numerical model of the multistage radial turbine.

where h_{tot} is the total enthalpy, related to the static enthalpy h by

$$h_{tot} = h_{stat} + \frac{1}{2} \vec{U}^2 \quad (6)$$

The term $\nabla \cdot (\vec{U} \cdot \tau)$ represents the work due to viscous stresses and is called the viscous work term. This model includes the internal heating by viscosity in the fluid, and is negligible in most flows.

The equation of k - ω shear stress transport turbulence (SST) model is defined as follows²⁶

$$\frac{\partial(\rho k)}{\partial t} + \nabla \cdot (\rho \vec{U} k) = \nabla \cdot \left[\left(\mu + \frac{\mu_t}{\sigma_{k3}} \right) \nabla k \right] + P_k - \beta' \rho k \omega \quad (7)$$

$$\begin{aligned} & \frac{\partial(\rho \omega)}{\partial t} + \nabla \cdot (\rho \vec{U} \omega) \\ &= \nabla \cdot \left[\left(\mu + \frac{\mu_t}{\sigma_{\omega 3}} \right) \nabla \omega \right] + (1 - F_1) 2\rho \frac{1}{\sigma_{\omega 2} \omega} \nabla k \nabla \omega \\ & \quad + \alpha_3 \frac{\omega}{k} P_k - \beta_3 \rho \omega^2 \end{aligned} \quad (8)$$

The coefficients of the new model are a linear combination of the corresponding coefficients of the underlying models. They can be defined as follows

$$\phi = F_1 \phi_1 + (1 - F_1) \phi_2 \quad (9)$$

All coefficients are given as follows

$$\begin{aligned} \beta' &= 0.09 & \alpha_1 &= 5/9 & \beta_1 &= 0.075 \\ \sigma_{k1} &= 2 & \sigma_{\omega 1} &= 2, & \alpha_2 &= 0.44, \\ \beta_2 &= 0.0828, & \sigma_{k2} &= 1, & \sigma_{\omega 2} &= 1/0.856 \end{aligned} \quad (10)$$

F_1 in equation (9) is defined as

$$F_1 = \tanh(\arg_1^4) \quad (11)$$

With

$$\arg_1 = \min \left[\max \left(\frac{\sqrt{k}}{0.09 \omega y}; \frac{500 \nu}{y^2 \omega} \right); \frac{4 \rho \sigma_{\omega 2} k}{CD_{k\omega} y^2} \right] \quad (12)$$

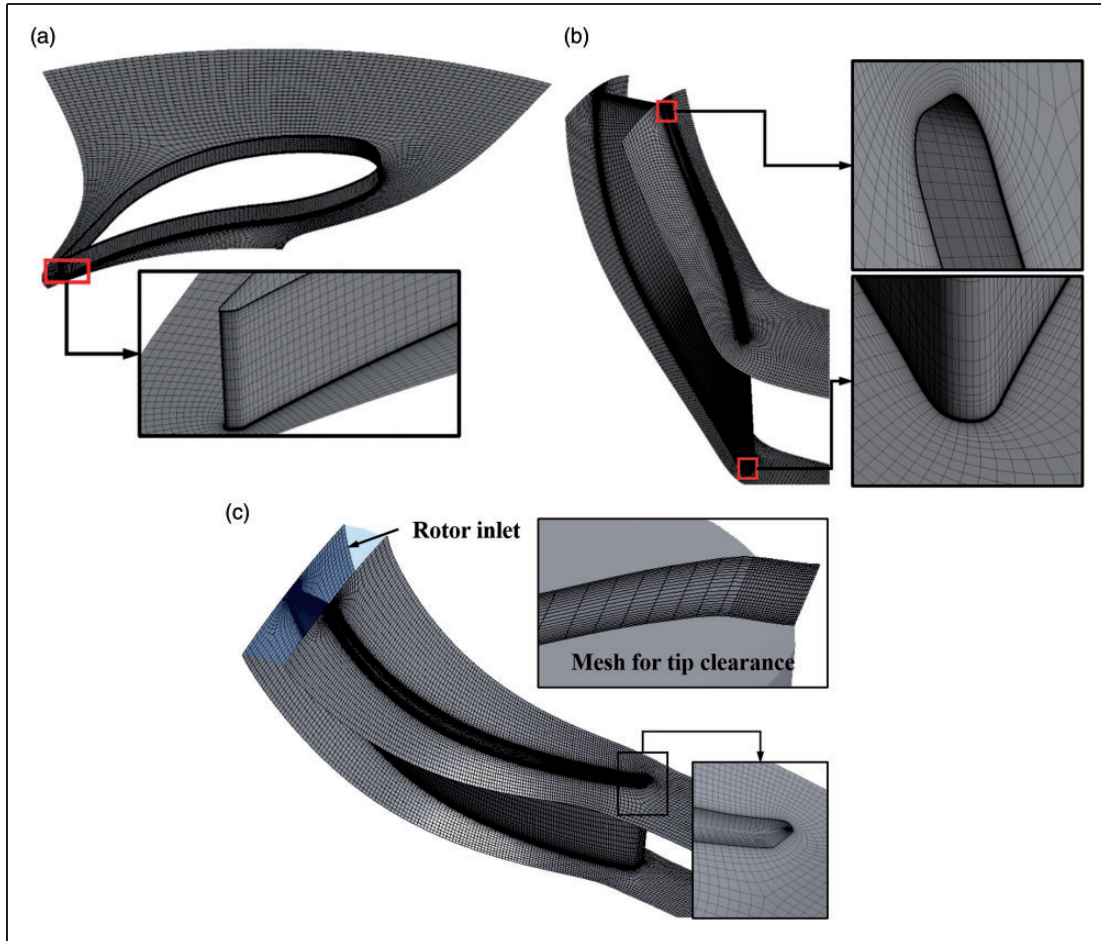


Figure 5. Computational mesh for the radial turbines: (a) mesh for the nozzle; (b) mesh for the shrouded rotor; (c) mesh for the unshrouded rotor.

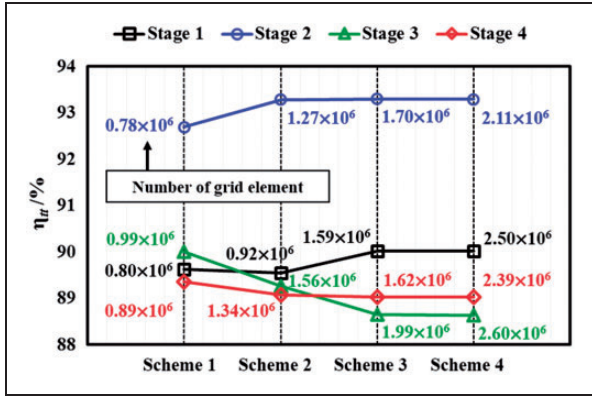


Figure 6. Grid validation for the four-stage radial inflow turbine.

where y is the distance to the nearest wall and ν is the kinematic viscosity and

$$CD_{k\omega} = \max\left(2\rho \frac{1}{\sigma_{\omega 2} \omega} \frac{\partial k}{\partial x_j} \frac{\partial \omega}{\partial x_j}, 10^{-10}\right) \quad (13)$$

In the SST model, the proper transport behavior can be obtained by a formulation of the eddy-viscosity

$$v_t = \frac{a_1 k}{\max(a_1 \omega; SF_2)} \quad (14)$$

where $v_t = \mu_t / \rho$.

F_2 in equation (14) is a blending function similar to F_1 , which restricts the limiter to the wall boundary layer, as the underlying assumptions are not correct for free shear flows. S is an invariant measure of the strain rate.

$$F_2 = \tanh(\arg_2^2) \quad (15)$$

$$\arg_2 = \max\left(2 \frac{\sqrt{k}}{\beta' \omega y}; \frac{500\nu}{y^2 \omega}\right) \quad (16)$$

The computational mesh for the numerical model is depicted in Figure 5. A structured grid is adopted for the stator and rotor domains. The grid is refined near the wall of the radial turbine and tip clearance of the blade to satisfy the requirements of the turbulence model. Generally, the minimum wall y^+ is less than 1.0.

Figure 6 shows the grid independence of the four radial turbines. It can be found that the total–total isentropic efficiency of stage 1 is almost unchanged as the grid element increases from 1.59×10^6 to 2.50×10^6 . In order to save the computing resource, the 1.59×10^6 grid elements are adopted for the computations of stage 1, and grid elements of 1.27×10^6 are adopted for stage 2. For the radial inflow turbine with unshrouded rotor, more grid elements are adopted in the tip clearance region. It can be seen in Figure 6 that the total–total isentropic efficiency of stage 3 remains invariant as the grid element increases

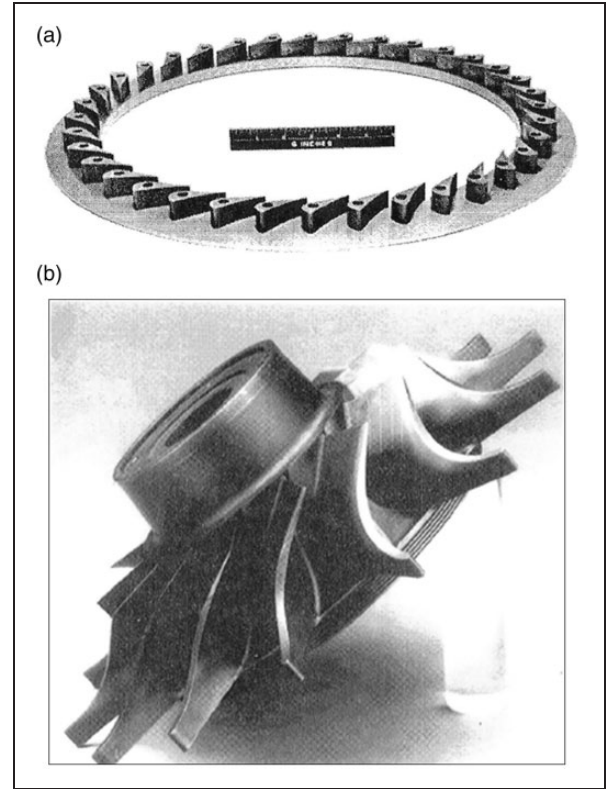


Figure 7. Geometry of the NASA radial turbine: (a) stator I; (b) rotor I.²⁷

Table 2. Performance comparison for NASA radial turbine.

| | Experiment | CFD | Relative error |
|-------------------------------|------------|--------|----------------|
| Mass flow (kg/s) | 2.71 | 2.70 | −0.36% |
| Total-to-total efficiency (%) | 88.50 | 90.88 | +2.70% |
| Output power (kW) | 424.30 | 435.52 | +2.64% |

CFD: computational fluid dynamics.

from 1.99×10^6 to 2.60×10^6 , so 1.99×10^6 grid elements are adopted for stages 3, and 1.62×10^6 grid elements are adopted for stage 4.

Results and discussion

Validation of the computational fluid dynamics model

Up to now, experimental data on the radial turbine operating in supercritical condition are limited, and the directly experiment validation of performance and flow structure in the supercritical radial turbine is difficult. In the present study, the National Aeronautics and Space Administration (NASA) compact inflow turbine is selected to validate the model for its similar operational principle and structural style, detailed geometric parameters and complete experimental data in the existing literatures.

Figure 7 depicts the geometry of the NASA compact inflow turbine.²⁷

Table 2 shows the overall performance comparison for NASA radial turbine. The relative errors for mass flow, total to total efficiency, and output power are -0.36%, 2.70%, and +2.64% respectively, which are within engineering permissible error range. These errors may be attributed to the adoption of circumferential average treatment at rotor-stator interface, adiabatic wall, and smooth channel in the CFD model.

Comparison of outlet parameter distributions are shown in Figure 8. It can be found that total-to-total efficiency, total pressure ratio, total temperature ratio, and flow angle obtained by numerical simulation present higher errors at 30–70% span location. This is mainly due to the exist of rotor back gap in the experiment.²³ Overall, the calculated distributions agree well with the experiental data.

Effects of gas model on the performance and flow pattern of radial turbine

The radial turbine of stage 1 is operated under the supercritical condition, and it is still not clear that the solution precision of the supercritical gas flow using ideal gas model. To provide reference for the analysis and design of radial turbine with similar

condition, the effects of gas model on the performance and the flow pattern of radial turbine is investigated in the present study.

Description of the gas models

Ideal gas model. For the ideal gas model in ANSYS CFX, density ρ is calculated from the ideal gas law and C_p is considered as a function of temperature. The thermodynamic parameters can be calculated as follows

$$\rho = \frac{wP_{abs}}{R_0T} \quad (17)$$

Table 3. Performance comparison of stage I using real gas property and ideal gas model.

| | Real gas property | Ideal gas model | Relative differences |
|-------------------------------------|-------------------|-----------------|----------------------|
| Mass flow (kg/s) | 5.01 | 4.99 | -0.39% |
| Total-to-total efficiency (%) | 89.26 | 87.74 | -1.70% |
| Output power (kW) | 425.41 | 385.59 | -9.36% |
| Isentropic drop of enthalpy (kJ/kg) | 95.13 | 88.13 | -7.36% |

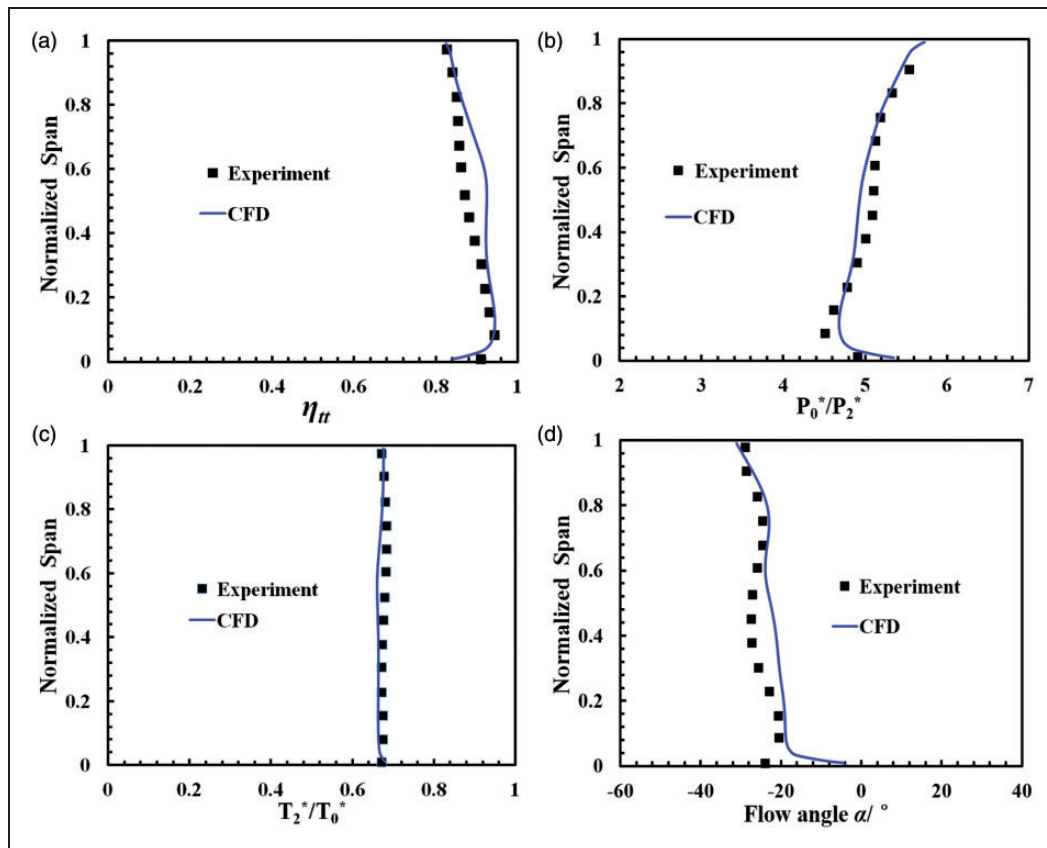


Figure 8. Comparison of the parameters distribution at outlet of rotor for NASA turbine: (a) total-to-total efficiency; (b) total pressure ratio; (c) total temperature ratio; (d) flow angle α .

$$dh = C_p dT \tag{18}$$

$$C_p = C_p(T) \tag{19}$$

$$s - s_{ref} = \int_{T_{ref}}^T \frac{C_p(T)}{T} dT - R \log\left(\frac{P}{P_{ref}}\right) \tag{20}$$

$$h_{stat} - h_{ref} = \int_{T_{ref}}^{T_{stat}} C_p(T) dT \tag{21}$$

where w is the molecular weight, P_{abs} is the absolute pressure, and R_0 is the universal gas constant.

For the ideal gas model in CFX, the specific heat C_p is expressed in polynomial form (equation (22)),

and the coefficient values a_i in the equation is determined based on Sonntag et al.²⁸

$$\frac{C_p}{R} = a_1 + a_2 T + a_3 T^2 + a_4 T^3 + a_5 T^4 \tag{22}$$

where R is the specific gas constant.

Real gas model. The real gas model of the compressed air is based on the gas physical property tables. In such a table, the thermodynamic property data of compressed air at given pressure and temperature are obtained by calling software REFPROP.²⁹

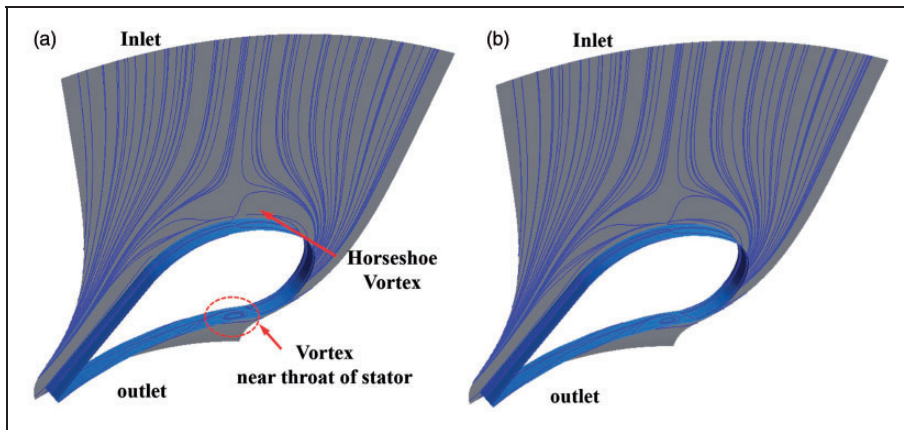


Figure 9. streamlines at surface of flow channel in stator: (a) real gas property; (b) ideal gas model.

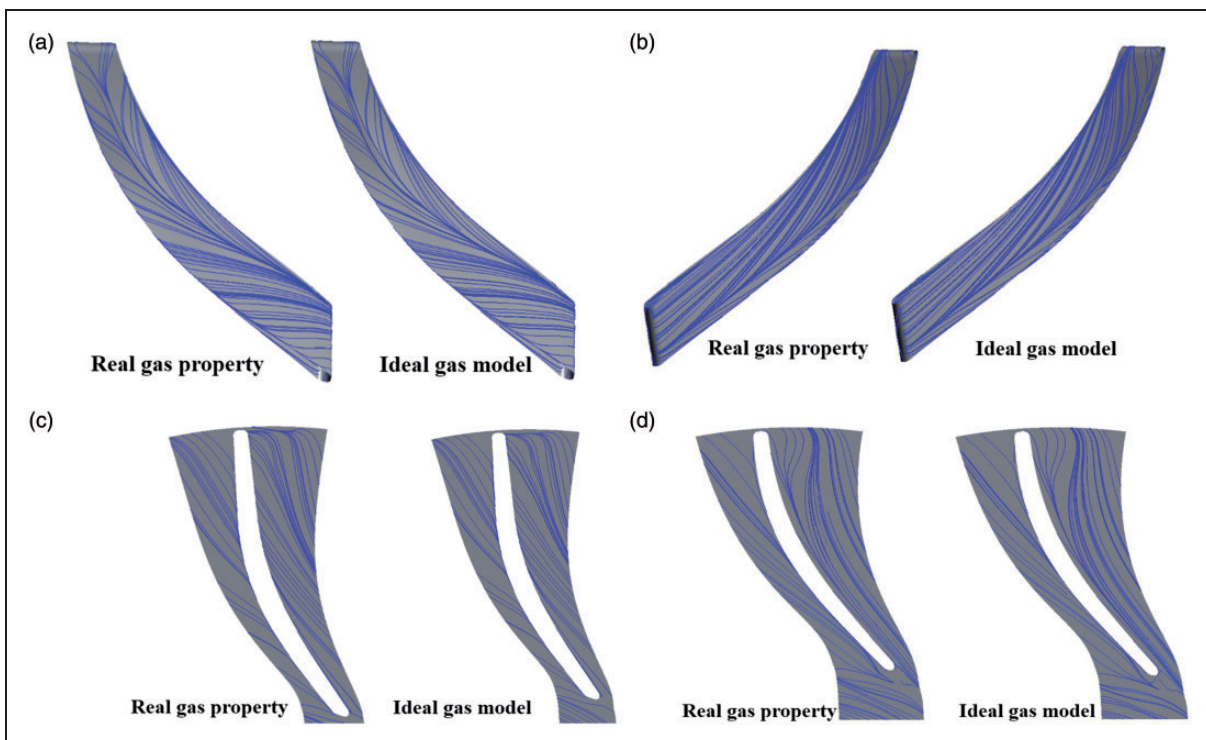


Figure 10. path lines on the surface of rotor: (a) suction surface; (b) pressure surface; (c) hub surface; (d) shroud surface.

These tables are integrated into an RGP file by using in-house developed code, and the RGP file is integrated into the software of ANSYS CFX to complete the CFD solution process. In this study, nine tables are adopted to describe the thermophysical properties, shown as follows

$$\begin{aligned} &h(P, T), c(P, T), v(P, T), C_V(P, T), C_P(P, T), \\ &(\partial P/\partial v)_T(P, T), s(P, T), \mu(P, T), k(P, T) \end{aligned} \quad (23)$$

Effects of gas model. Table 3 shows the performance comparison of stage 1 by using real gas property and ideal gas model. The relative differences of the mass flow is 0.39%, relative differences of output power is 9.36%, which is much higher. The isentropic efficiency is determined by the ratio of actual enthalpy drop and isentropic enthalpy drop. When the ideal gas model is employed, the deviations for the isentropic enthalpy drop and actual enthalpy drop in similar proportion. In Table 3, the relative differences for isentropic drop of enthalpy is -7.36%, the relative differences for actual drop of enthalpy, which can be derived from mass flow and output power, is -9%. Thus, the relative difference for total to total efficiency

is -1.7%, which is small. Same results can also be observed in Zhang et al.³⁰

Figures 9 and 10 depict the streamlines on the surface of stator and rotor obtained by using real gas property and ideal gas model. It can be found that the distribution of streamlines obtained by the two models is nearly the same. The shape and location of horseshoe vortex and the vortex near throat of stator is almost identical. In the rotor, the topological structure of streamline on the suction and pressure surface of blade, hub, and shroud are also nearly the same. These results illustrate that the ideal gas model has little effect on the flow pattern under supercritical condition.

Figure 11 depicts the distribution of static entropy, Mach number, and pressure in the rotor. It can also be found that static entropy, Mach number, and pressure in the stator obtained by the two models are also nearly the same. As shown in Figure 12, the distribution of inlet-to-exit total pressure ratio, inlet-to-exit Mach number at outlet of rotor are also similar, while higher entropy and lower inlet-to-exit total temperature ratio are obtained when ideal gas model is adopted.

To provide further explanation, comparison of thermodynamic parameters between real gas property and ideal gas model is shown in Figure 13.

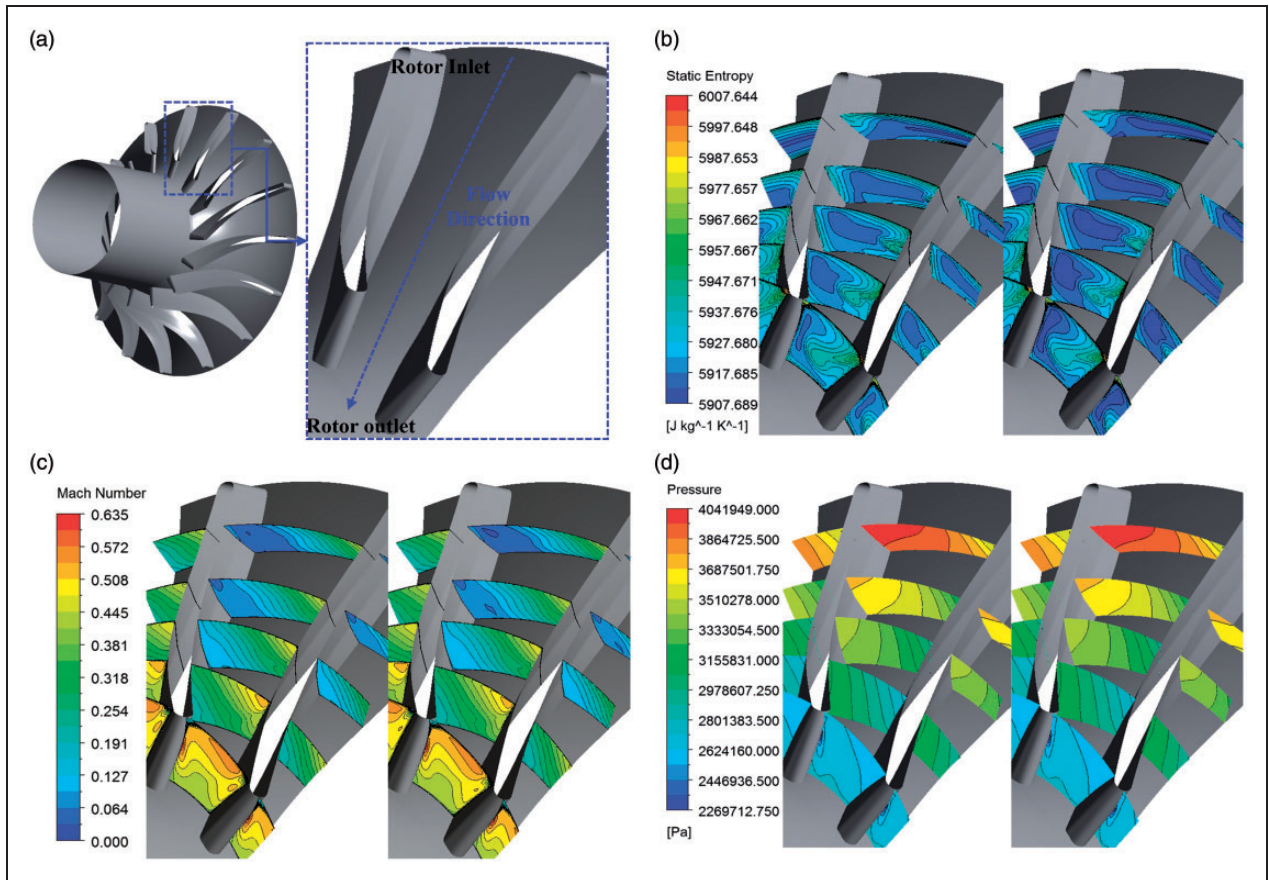


Figure 11. Distribution of static entropy, Mach number, and pressure in the rotor: (a) sketch of observe location; (b) static entropy distribution; (c) Mach number distribution; (d) pressure distribution.

As shown in Figure 13(a), the specific volume–pressure curve obtained by ideal gas model is almost consistent with that of real gas property when compressed air reaches supercritical condition ($P > 3.85$ MPa, $T > 132.83$ K), thus the expansion processes obtained by the two models are nearly the same and result in similar flow structure and

path line distribution in Figures 9 and 10. In Figure 13(b), the specific heat capacity at constant pressure C_p increases with the increase of temperature for ideal gas model. However, it decreases with the increase of temperature when real gas property is adopted. In ideal gas model, static entropy and enthalpy are calculated from C_p by equations (20)

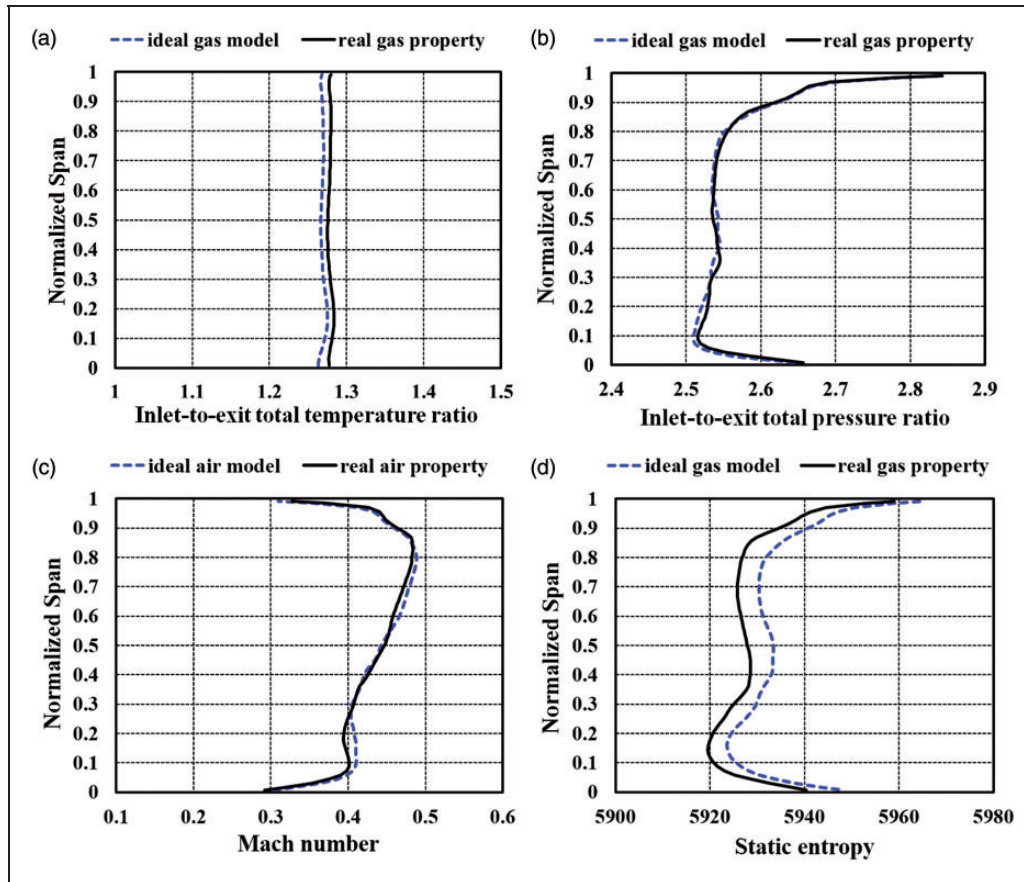


Figure 12. Comparison of rotor outlet parameters between real gas property and ideal gas model: (a) inlet-to-exit total temperature ratio; (b) inlet-to-exit total pressure ratio; (c) Mach number; (d) static entropy 改为 temperature ratio.

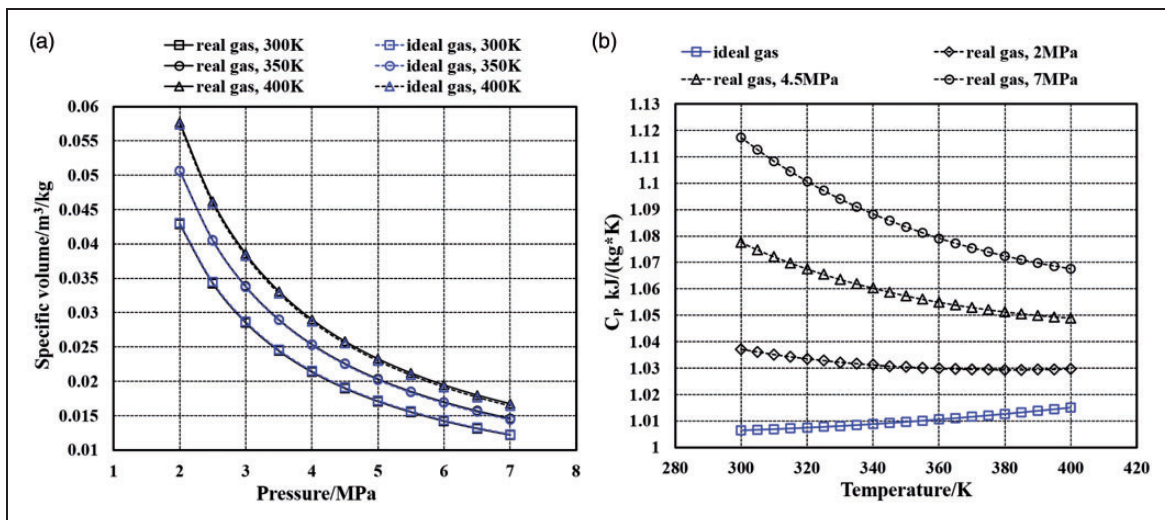


Figure 13. Comparison of thermodynamic parameters between real gas property and ideal gas model: (a) variation of specific volume with pressure; (b) variation of C_p with temperature.

and (21), respectively. And thus, the obvious deviation of isentropic enthalpy drop, inlet-to-exit total temperature ratio and entropy are observed in Table 3, Figure 12(a), and in Figure 12(d), respectively.

Analysis on aerodynamic performance and flow field of multistage radial turbines

Internal flow and loss in the stators. The entropy contours in the stators of the four stages are analyzed in

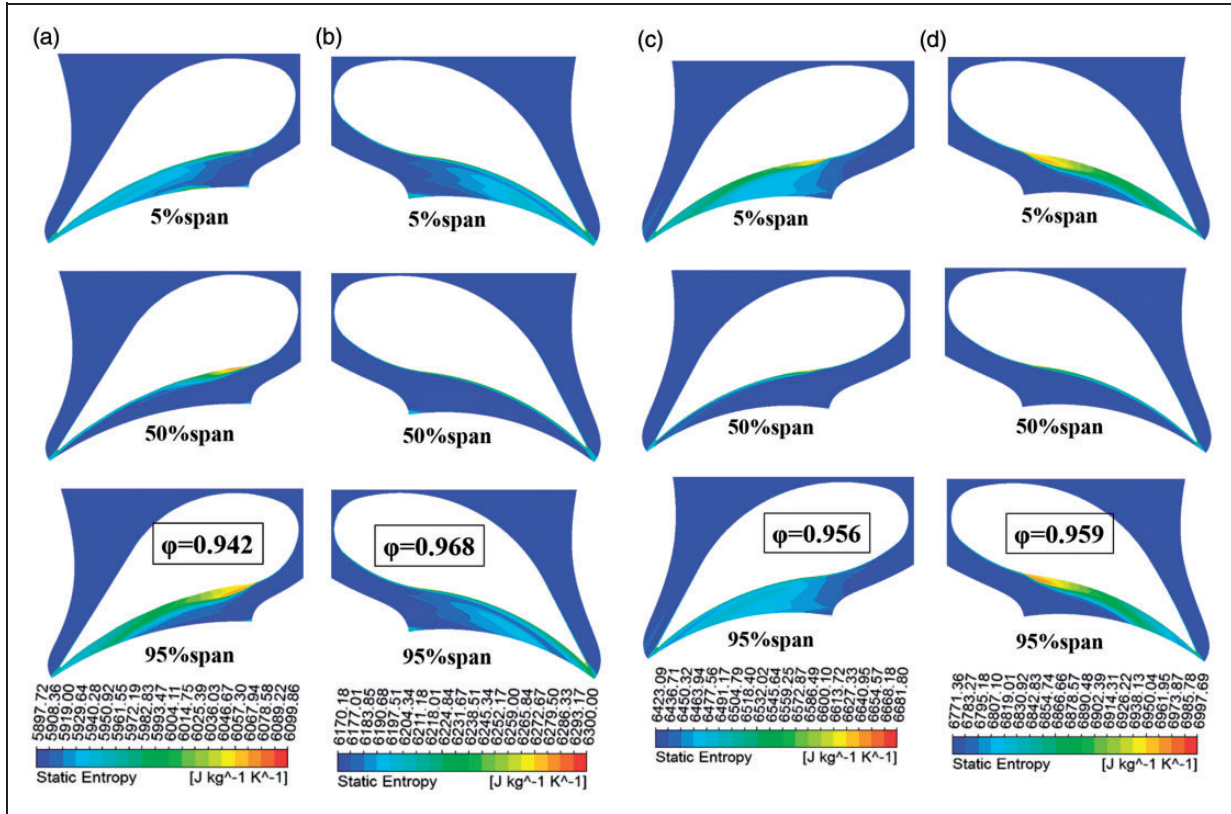


Figure 14. Entropy contours in the stators of the four stages: (a) stage 1; (b) stage 2; (c) stage 3; (d) stage 4.

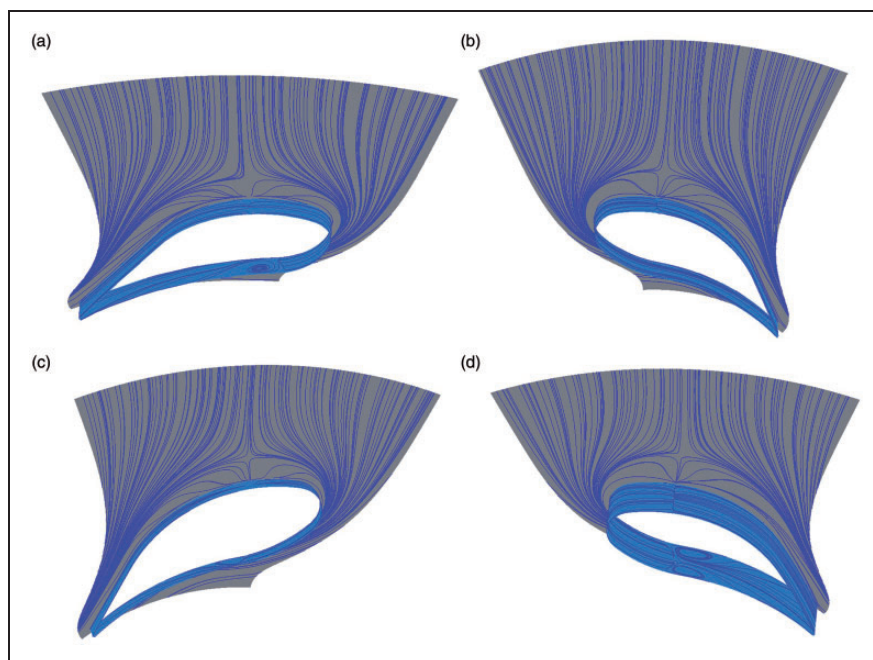


Figure 15. path lines on the surface of stators of the four stages: (a) stage 1; (b) stage 2; (c) stage 3; (d) stage 4.

Figure 14. For all of the stages, the region near the hub and shroud (5% span and 95% span) presents higher entropy compared to the region at 50% span. At the throat region, the entropy at 50% span of stator in stage 1 is obviously higher than that in other stages, which explains why the velocity coefficient φ of stator in stage 1 is the lowest among the stages. The velocity coefficient of the stator φ is defined as

$$\varphi = \frac{c_1}{c_0} = \frac{c_1}{\sqrt{2(h_0^* - h_{1,s})}} \quad (24)$$

Figure 15 depicts the streamlines on the surface of stators of the four stages. A vortex, which lead to higher flow loss, can be found at the throat region of the stator exist in all of the stages, except for stage 2. It explains why the velocity coefficient φ of stator in stage 2 is the highest among the stages. For manufacturing easily, the present profiles of the stators for the four stages are constituted by arcs (front part of the stators) and straight lines (trail part of the stators). They increase the adverse pressure gradient at outlet of stage 1, stage 3 and stage 4 stators and thereby generate vortices, which are shown in

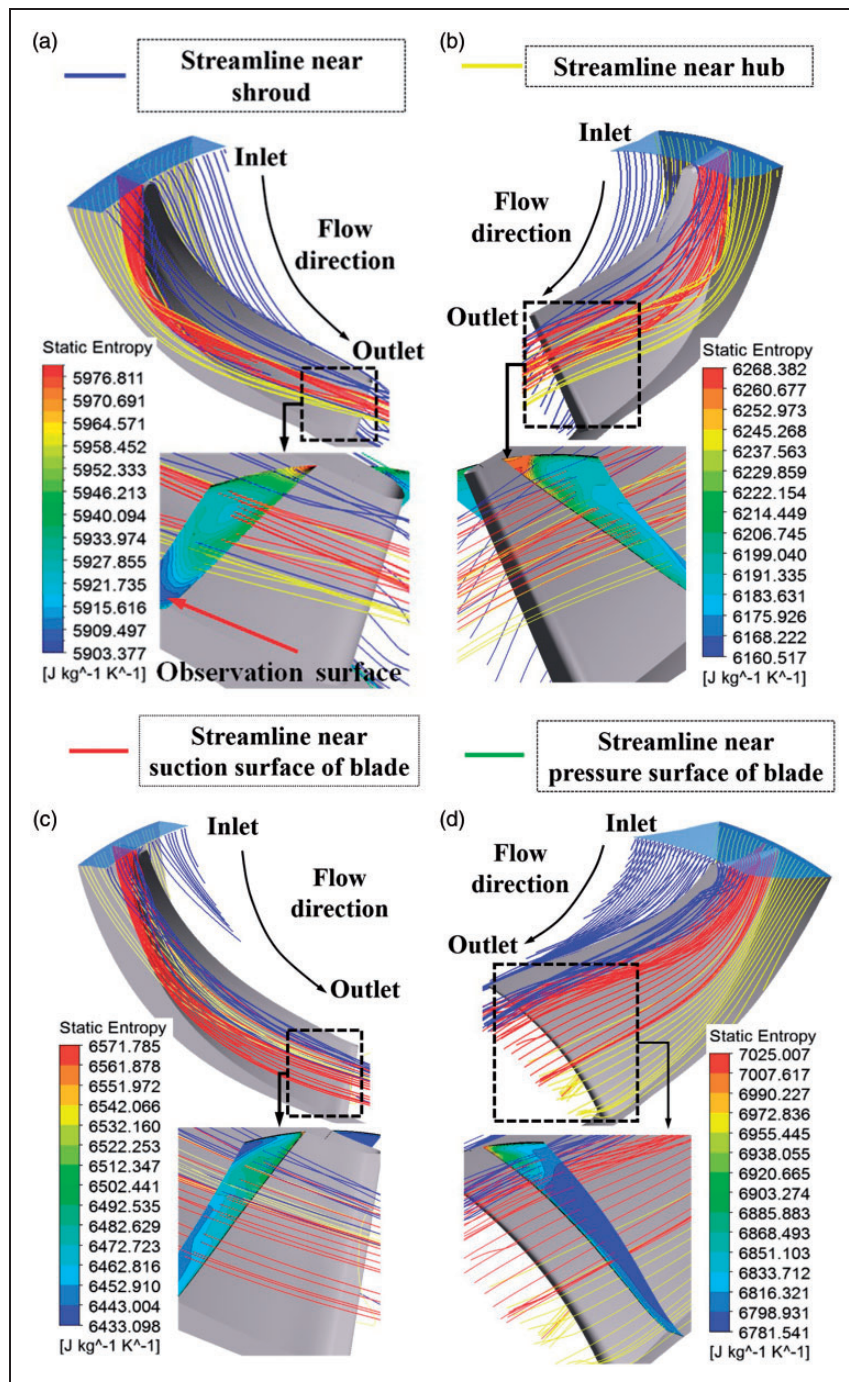


Figure 16. Internal flow and loss near suction surface of blade in the shrouded rotor: (a) stage 1; (b) stage 2; (c) stage 3; (d) stage 4.

Figure 15(a), (c), and (d), the flow loss and static entropy shown in Figure 14(a), (c), and (d) is thus increased by these vortices.

Internal flow and loss in the rotors. Shrouded and unshrouded rotors have been widely used in the field of radial turbines. In the present study, both of them are also adopted and investigated. Figure 16 depicts the internal flow and loss near suction surface of blade in shrouded rotor. It can be found that the working fluid near the shroud sweeps down the span and mixes with the working fluid near the suction surface of the

blade, and the working fluid near the hub also rolls up and mixes with these working fluids near the suction surface of the blade. The corresponding entropy contours further illustrate that the mixing of the working fluid near the hub, blade suction surface and the shroud is the main influence factor of the flow loss in shrouded rotor.

Figure 17 depicts the internal flow and loss near suction surface of blade in the unshrouded rotor. The working fluid near the pressure side of the blade passes through the tip clearance to form the leakage vortex, which mainly concentrated near

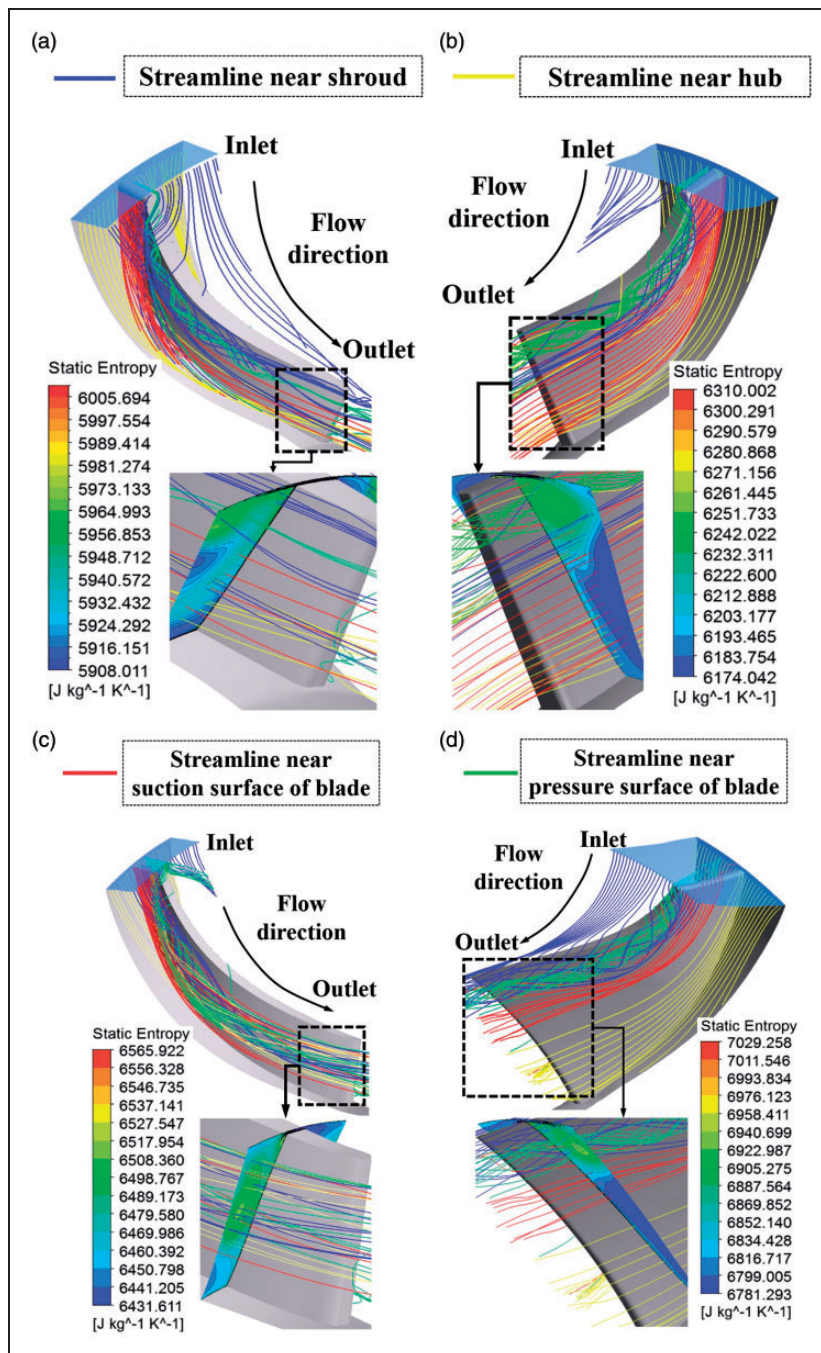


Figure 17. Internal flow and loss near suction surface of blade in the unshrouded rotor: (a) stage 1; (b) stage 2; (c) stage 3; (d) stage 4.

the suction side of the blade. It also mix with the fluid deriving from the shroud and suction surface (Figure 17(a) and (c)). For stages 2 and 4, the fluid deriving from the hub is also mixed with the leakage vortex. As a result, the flow loss corresponding to the leakage vortex is much higher in the rotor.

To further compare the internal flow in shrouded and unshrouded rotors, spanwise distribution of flow

angle and isentropic efficiency distribution on the observe surface is provided in Figures 18 and 19. The definition for the efficiency at observation surface is shown below

$$\eta_{observ} = \frac{h_0^* - h_{observ}^*}{h_0^* - h_{observ,S}^*} \quad (25)$$

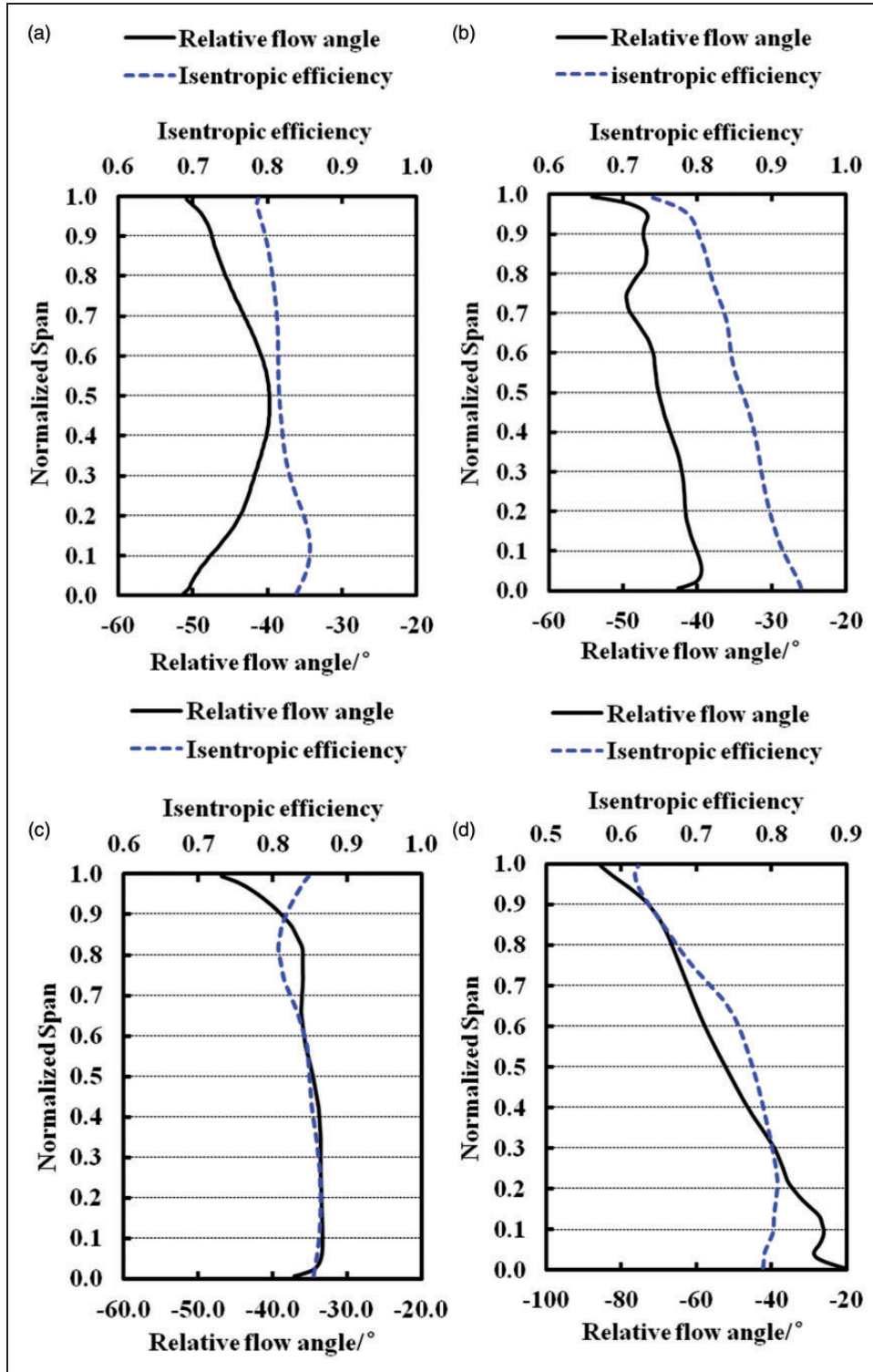


Figure 18. The flow angle and efficiency distribution at outlet of shrouded rotor: (a) stage 1; (b) stage 2; (c) stage 3; (d) stage 4.

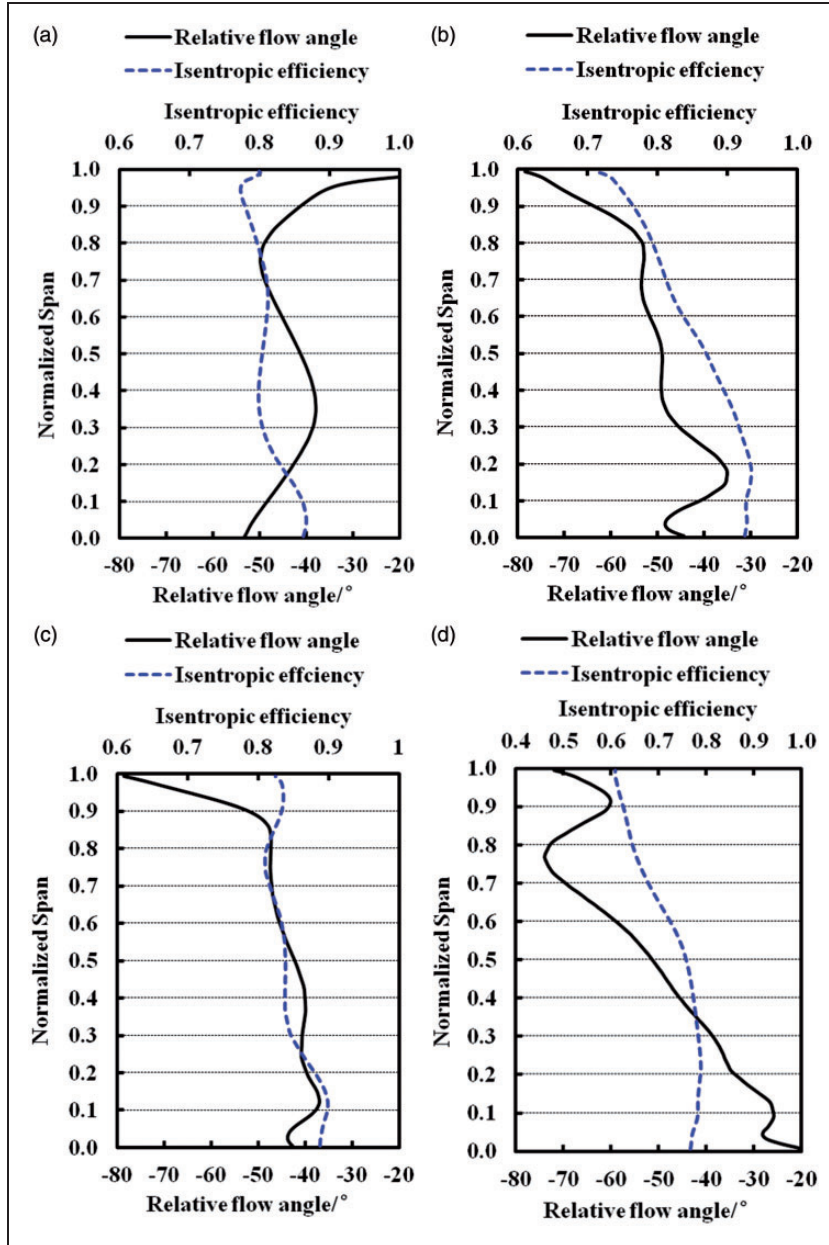


Figure 19. The flow angle and efficiency distribution at outlet of unshrouded rotor: (a) stage 1; (b) stage 2; (c) stage 3; (d) stage 4.

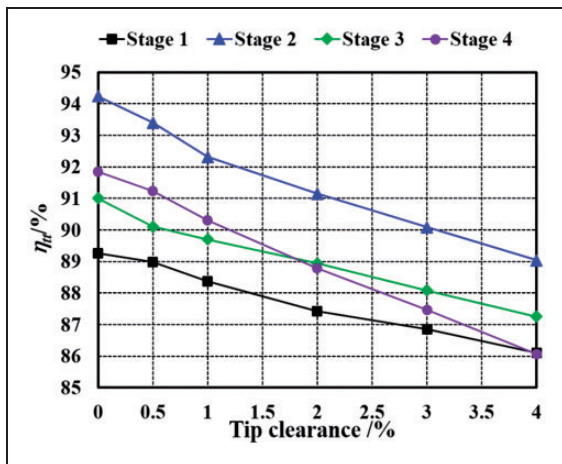


Figure 20. Variation of η_{tt} of the four stages with tip clearance.

where h_{observ}^* is the isentropic total enthalpy at observation surface; $h_{observ,S}^*$ represents the isentropic total enthalpy at observation surface, both of them are calculated in relative rotational coordination.

For both of shrouded and unshrouded rotors, the isentropic efficiency in high entropy region present lower value and decrease along blade height. It illustrated that the flow loss mainly concentrates near the blade tip region. Compared to shrouded rotors, more complex and obvious variation for isentropic efficiency and flow angle is observed in the unshrouded rotors because of the existence of tip leakage vortex.

Effects of tip clearance on performance and internal flow of radial turbine. From the above analysis, tip clearance plays an important role on the aerodynamic performance and flow pattern of radial turbine, and the effects

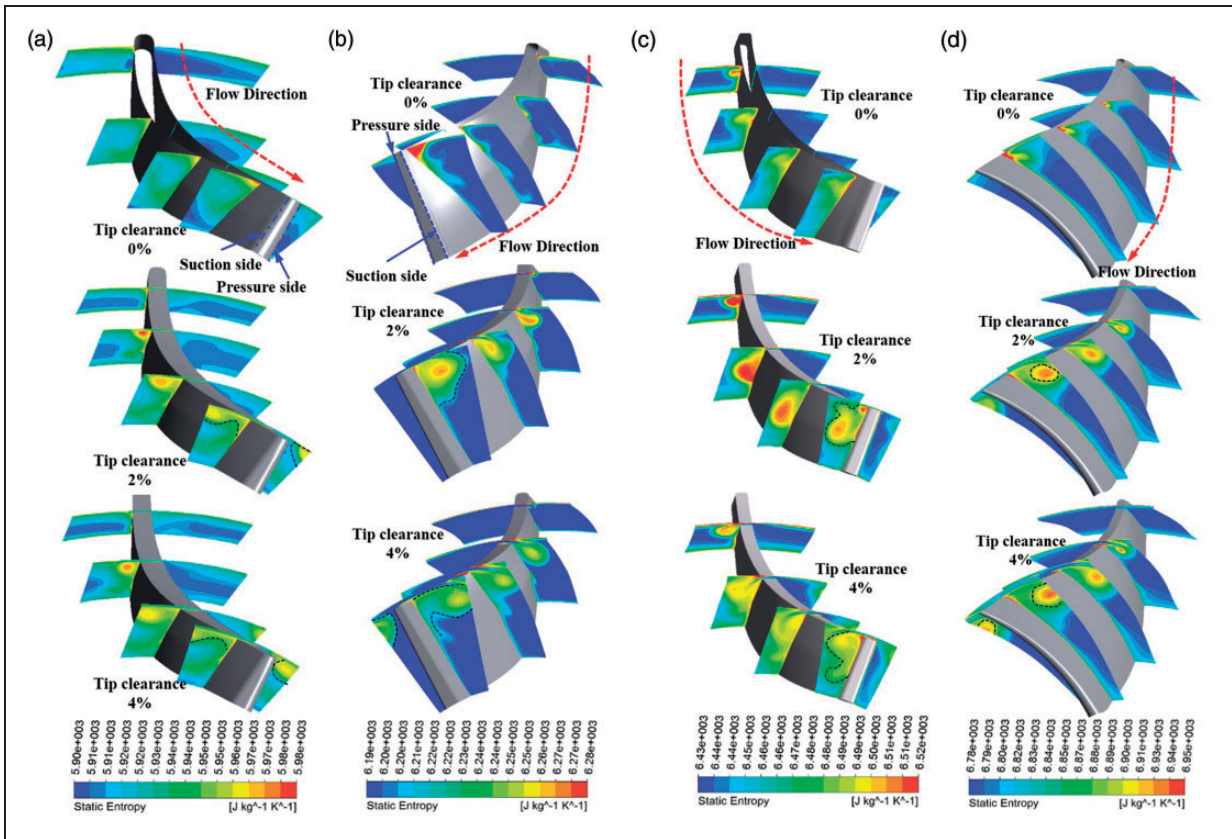


Figure 21. Entropy contour in the rotor of the four stages: (a) stage 1; (b) stage 2; (c) stage 3; (d) stage 4.

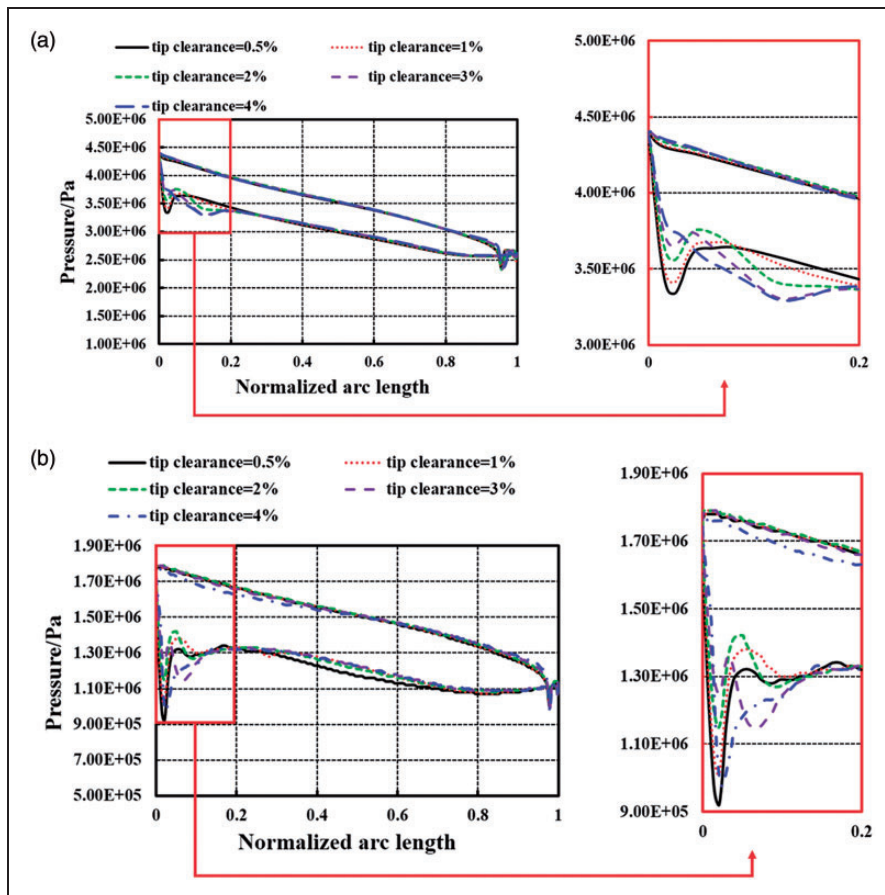


Figure 22. Pressure distribution at blade surface of rotor near tip clearance (90% span): (a) stage 1; (b) stage 2; (c) stage 3; (d) stage 4.

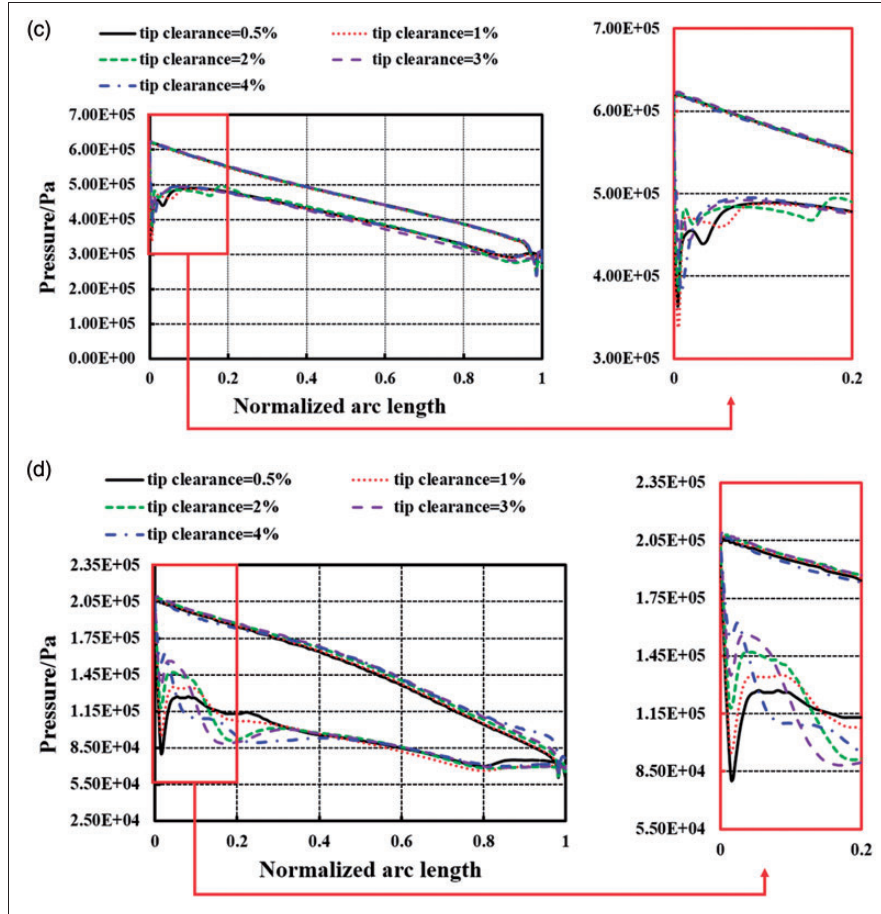


Figure 22. Continued.

of tip clearance height on the total-to-total efficiency η_{tt} of the four stages are investigated. The tip clearance height, which is shown in Figure 3(a), is defined by the percentage of rotor blade height at outlet. And it keeps constant from the inlet to the outlet of the rotor. The total-to-total efficiency of radial turbines is defined as

$$\eta_{tt} = \frac{h_0^* - h_2^*}{h_0^* - h_{2,S}^*} \quad (26)$$

where h_2^* is the isentropic total enthalpy at observation surface; $h_{2,S}^*$ represents the isentropic total enthalpy at outlet of rotors.

As shown in Figure 20, total-to-total efficiency η_{tt} for all of stages decreased with the increase of the tip clearance height. However, when the tip clearance height increases from 0% to 4%, the total-to-total efficiencies of stage 1, stage 2, stage 3, and stage 4 are reduced by 3.17%, 5.2%, 3.75%, and 5.78%, respectively. By comparing the parameters in Table 1, it can be found that stages 2 and 4, which have higher value of χ , present higher efficiency reduction compared to that of stages 1 and 3.

The entropy contour corresponding to the flow loss in the rotor of the four stages is shown in Figure 21.

For all of the stages, the high entropy region moves to the pressure surface of the adjacent blade with the increase of the tip clearance height, the influence range is also increased, and the total-to-total isentropic efficiency η_{tt} is thus decreased. For the rotor of stages 2 and 4, the influence range of high entropy region (marked with dotted lines) increases more obviously. That is why stages 2 and 4 present higher efficiency reduction.

Pressure distribution at blade surface of rotor near tip clearance (90% span) is shown in Figure 22. For the rotors of stages 2 and 4, the pressure fluctuation on the suction surface at the leading edge of the blade is more obvious. This is because the blade with higher value of χ also has higher blade height difference between inlet and outlet of rotor, and the proportion of tip clearance in the blade inlet height is thus increased. Therefore, leakage flow at leading edge of rotor is increased, and more serious pressure fluctuation is observed.

Conclusion

The present study firstly conducted a numerical simulation of a multistage radial turbine of CAES. Influence of ideal gas model on the radial turbine

(stage 1) operated under supercritical condition is analyzed. Internal flow structure and loss of the four stages are revealed, and effects of tip clearance on the four radial inflow turbines are also investigated. The following conclusions were obtained:

1. The ideal gas model can qualitatively describe the real flow pattern under supercritical condition, while leading to obvious deviation of isentropic enthalpy drop, entropy, and inlet-to-exit total temperature ratio. Relative differences of mass flow is -0.39%, relative differences of efficiency is -1.70%, and relative differences of output power is -9.36%.
2. For shrouded rotor, mixing of the working fluid near the hub, blade suction surface, and the shroud are the main influencing factors of the flow loss in the rotor. For unshrouded rotor, the leakage vortex, which promote the mixture of the fluid deriving from the hub, shroud, and suction surface, mainly influence the flow loss in the channel of rotor.
3. When the tip clearance height increased from 0% to 4%, it can be found that high entropy region in the four rotors moves to the pressure surface of the adjacent blade. Besides, rotors in stages 2 and 4 present higher efficiency reduction compared to that of the rotors in stages 1 and 3. This is because the rotors in stages 2 and 4 has higher blade height variation rate. Such structural characteristic increases the proportion of tip clearance in blade inlet height, cause more serious leakage flow at leading edge of rotor, and results in more serious pressure fluctuation and higher efficiency reduction.

Finally, further profile optimization will be conducted in our future work to suppress the flow loss in the stators.

Declaration of Conflicting Interests

The author(s) declared no potential conflicts of interest with respect to the research, authorship, and/or publication of this article.

Funding

The author(s) disclosed receipt of the following financial support for the research, authorship, and/or publication of this article: National Natural Science Foundation of China (grant no. 51522605), National Natural Science Foundation of China (grant no. 51406206), Key Project of Chinese National Programs for Fundamental Research, Development (973 program) (grant no. 2015CB251302), and CAS Interdisciplinary Innovation Team Fund.

References

1. Palizban O and Kauhaniemi K. Energy storage systems in modern grids—Matrix of technologies and applications. *J Energy Storage* 2016; <http://dx.doi.org/10.1016/j.est.2016.02.001>.
2. Georges Salgi G and Lund H. System behavior of compressed-air energy-storage in Denmark with a high penetration of renewable energy sources. *Appl Energy* 2008; 85: 182–189.
3. Safaei H, Keith DW and Hugo RJ. Compressed air energy storage (CAES) with compressors distributed at heat loads to enable waste heat utilization. *Appl Energy* 2013; 103: 165–179.
4. Budt M, Wolf D and Span R. A review on compressed air energy storage: Basic principles, past milestones and recent developments. *Appl Energy* 2016; 170: 250–268.
5. Ma C and Yuan X. Investigation of unsteady flow in a single stage high load radial turbine by 3D RANS simulation. *J Eng Thermophys* 2012; 33: 757–760.
6. Alexin Putra M and Joos F. Investigation of secondary flow behavior in a radial turbine nozzle. *J Turbomach* 2013; 135: 061003-1–061003-11.
7. Zangeneh-kazemi M, Dawes WN and Hawthorne WR. Three dimensional flow in radial-inflow turbines. In: *ASME 1988 international gas turbine and aeroengine congress and exposition*, Amsterdam, The Netherlands, 6–9 June 1988, paper no. 88-GT-103.
8. Dai R and Chen K. Numerical investigation of the fluid inside radial inflow turbine. *Therm Turbine* 2004; 33: 184–189.
9. Simpson AT, Spence SWT and Watterson JK. A comparison of the flow structures and losses within vaned and vaneless stators for radial turbines. *J Turbomach* 2009; 131: 031010-1–031010-15.
10. Binder N, Le Guyader S and Carbonneau X. Analysis of the variable geometry effect in radial turbines. *J Turbomach* 2012; 134: 041017-1–041017-9.
11. He P, Sun Z and Guo B. Aerothermal investigation of backface clearance flow in deeply scalloped radial turbines. *J Turbomach* 2013; 135: 021002-1–021002-12.
12. Li H, Deng Q, Fu L, et al. Numerical investigation on three-dimensional complexity flows in a wheel of radial inflow turbine. *J Eng Thermophys* 2012; 33: 945–948.
13. Li We, Wan Y, Zhang X, et al. Simulation of the flow in a radial inflow turbine of one micro turbine engine. *J Changchun Univ Sci Technol* 2016; 39: 78–82.
14. Amedick V and Simon H. Numerical simulation of the flow through the rotor of a radial inflow turbine. In: *ASME 1997 international gas turbine and aeroengine congress and exhibition*, Orlando, FL, USA, 2–5 June 1997, paper no. 97-GT-090.
15. Deng QH, Niu JF and Feng ZP. Effects of rotor blade tip clearance on total aerodynamic performance in a radial inflow turbine. *J Eng Thermophys* 2006; 27: 408–410.
16. Guo H, Xu YJ and Chen HS. Thermodynamic characteristics of a novel supercritical compressed air energy storage system. *Energy Convers Manage* 2016; 115: 167–177.
17. Larosiliere LM. Navier-Stokes analysis of radial turbine rotor performance. NASA Contract Report 191153, 1993.
18. Fu L, Shi Y and Deng Q. Integrated optimization design for a radial turbine wheel of a 100 kW-class microturbine. *J Eng Gas Turbines Power* 2012; 134: 012301-1–012301-8.
19. Okapuu U and Calvert GS. Cooled radial turbine for high power-to-weight applications. *J Aircraft* 1970; 7: 348–354.

20. Mueller L, Alsalihi Z and Verstraete T. Multidisciplinary optimization of a turbocharger radial turbine. *J Turbomach* 2013; 135: 021022-1–021022-9.
21. Jones AC. Design and test of a small high pressure ratio radial turbine. *J Turbomach* 1996; 118: 362–370.
22. Snyder PH and Roelke RJ. Design of an air-cooled metallic high-temperature radial turbine. *J Propul* 1990; 6: 283–288.
23. He P. *Investigation on the backface clearance flows in deeply scalloped radial turbines*. China: University of Chinese Academy of Sciences, 2012.
24. Li Y and Zheng Q. Numerical simulation of a multi-stage radial inflow turbine. In: *ASME turbo expo 2006: Power for land, sea and air*, Barcelona, Spain, 8–11 May 2006, paper no. GT2006-9137.
25. ANSYS Academic Research, Release 14.5, Theory Manual, ANSYS, Inc., Canonsburg, PA.
26. Menter FR. Two-equation eddy-viscosity turbulence models for engineering applications. *AIAA J* 1994; 32: 1598–1605.
27. Simonyi SP, Roelke JR, Stabe GR, et al. Aerodynamic evaluation of two compact radial inflow turbine rotors. NASA STI/Recon Technical Report 3514.
28. Sonntag RE, Borgnake C and Van Wylen GJ. *Fundamentals of thermodynamics*. 6th ed. New York: John Wiley & Sons Inc., 2003.
29. Lemmon EW, Huber ML and McLinden, MO. NIST reference fluid thermodynamic and transport properties—REFPROP[EB/OL]. NIST Standard Reference Database 23, Version 9.1, 2013.
30. Zhang L, Zhuge W and Zhang Y. The influence of real gas effects on ice-ORC turbine flow fields. In: *Proceedings of ASME turbo expo 2014: Turbine technical conference and exposition*, Düsseldorf, Germany, 2014.

| | |
|-------------|--------------------------|
| D | diameter |
| h | static enthalpy |
| k | turbulent kinetic energy |
| l | length |
| P | pressure |
| n | rotational speed |
| \dot{m} | mass flow rate |
| R | gas constant |
| s | entropy |
| \dot{S}_M | momentum source term |
| \dot{S}_E | energy source term |
| T | temperature |
| t | time |
| U | velocity |
| v | specific volume |
| w | molecular weight |
| η | efficiency |
| ω | turbulence frequency |

Subscripts

| | |
|---------------|-----------------------|
| 0 | stator inlet |
| 1 | state at rotor inlet |
| 2 | state at rotor outlet |
| <i>abs</i> | absolute |
| <i>Axial</i> | axial |
| <i>in</i> | inlet |
| <i>observ</i> | observation surface |
| <i>ref</i> | reference |
| <i>S</i> | isentropic process |
| <i>stat</i> | static |
| <i>tot</i> | total |
| <i>tt</i> | total-to-total |

Appendix

Notation

| | |
|-------|---|
| c | absolute velocity |
| C_P | specific heat capacity at constant pressure |

Superscript

| | |
|---|------------------|
| * | stagnation state |
|---|------------------|